






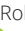












Gold nanorod–assisted theranostic solution for nonvisible residual disease in bladder cancer

Paolo Armanetti^{a,1} , Irene Locatelli^{b,c,1} , Chiara Venegoni^{b,c} , Elisa Alchera^{b,c}, Beatrice Campanella^d, Filippo Pederzoli^{b,c,e} , Mirko Maturif, Erica Locatelli^f , Silvia Tortorella^f , Flavio Curnis^g , Angelo Corti^g , Roberta Lucianò^h, Massimo Onorè^d , Andrea Salonia^{b,c,e} , Francesco Montorsi^{b,c,e} , Marco Moschini^{b,c}, Viktor Popovⁱ, Jithin Joseⁱ , Mauro Comes Franchini^{f,2} , Ean Hin Ooi^{k,2} , Luca Menichetti^{a,2} , and Massimo Alfano^{b,c,2} 

Affiliations are included on p. 11.

Edited by Guru Sonpavde, University of Central Florida, Orlando, FL; received June 10, 2024; accepted August 6, 2024 by Editorial Board Member Rakesh K. Jain

Residual nonvisible bladder cancer after proper treatment caused by technological and therapeutic limitations is responsible for tumor relapse and progression. This study aimed to demonstrate the feasibility of a solution for simultaneous detection and treatment of bladder cancer lesions smaller than one millimeter. The $\alpha 5\beta 1$ integrin was identified as a specific marker in 81% of human high-grade nonmuscle invasive bladder cancers and used as a target for the delivery of targeted gold nanorods (GNRs). In a preclinical model of orthotopic bladder cancer expressing the $\alpha 5\beta 1$ integrin, the photoacoustic imaging of targeted GNRs visualized lesions smaller than one millimeter, and their irradiation with continuous laser was used to induce GNR-assisted hyperthermia. Necrosis of the tumor mass, improved survival, and computational modeling were applied to demonstrate the efficacy and safety of this solution. Our study highlights the potential of the GNR-assisted theranostic strategy as a complementary solution in clinical practice to reduce the risk of nonvisible residual bladder cancer after current treatment. Further validation through clinical studies will support the findings of the present study.

bladder tumor | nanoparticles | photoacoustic imaging | hyperthermia | computational modeling

Bladder cancer (BC) is the tenth most common cancer worldwide, with more than half a million new diagnoses and 200,000 deaths every year (1). Approximately 75% of patients who are first diagnosed with BC have tumors confined either to the urothelium (noninvasive papillary carcinoma—Ta, and in situ carcinoma—CIS) or to the lamina propria (T1) and are classified as nonmuscle invasive bladder cancer (NMIBC) (2). Guidelines for the clinical management of NMIBC involve endoscopic transurethral resection of bladder tumor (TURBT), usually followed by intravesical instillation of adjuvant therapy (3). Unfortunately, patients with NMIBC often have a high tumor recurrence rate. At the second-look TURBT (i.e., <90 d after the first TURBT), residual high-grade disease was still detected in 40% of patients, with high-grade Ta making up the majority of these cases (57%) (4).

Even the use of the photodynamic diagnosis method (performed using blue light after preoperative intravesical instillation of hexaminolevulinic acid) concomitant to TURBT and early intravesical instillation of mitomycin C did not effectively reduce the frequency of NMIBC relapse, which stands up to 60% 3 y post-TURBT (5). Hence, more than 200,000 NMIBC patients each year are expected to have BC relapses, which often require multiple intervention sessions/cycles and follow-ups in an attempt to eradicate the tumor. This, coupled with the high cost involved in TURBT (6), results in BC becoming the most expensive malignancy to treat over the lifetime of patients, with an annual expenditure of USD 10 billion (7, 8). Consequently, reducing the recurrence rate of NMIBC relapses is a priority to improve quality of life and reduce the economic burden on patients and their caregivers.

To improve the success of clinical management of NMIBC, two limitations need to be addressed. First, photodynamic diagnosis is ineffective in detecting tumors smaller than 1 mm, with a specificity that is lower than white light endoscopy (63% vs. 81%). This is because photodynamic diagnosis can also detect areas of inflammation following TURBT or BCG instillation (9–11). This technical problem becomes even more severe when diagnosing bladder CIS due to its velvet-like appearance and with few neoplastic cells in a reddish area that is indistinguishable from inflammation. For tumors <1 mm in size, bladder lesions cannot be diagnosed using imaging methods, such as CT urography, intravenous urography (IVU), ultrasound (US), and multiparametric MRI (mpMRI), including the VI-RADS protocol (12), and the recently described high-frequency

Significance

Residual disease in bladder cancer is responsible for tumor recurrence and progression and is caused by technological and therapeutic limitations. This study demonstrated the feasibility of a theranostic solution represented by the intravesical instillation of urine-stable gold nanorods as a contrast agent for photoacoustic imaging and assisted hyperthermia via the photothermal effect. The solution allowed the detection of lesions <1 mm and killing of tumor cells by necrosis. The nanoparticles are targeted against the tumor-specific integrin $\alpha 5\beta 1$, expressed by the neoplasia in the preclinical model and 81% of high-grade nonmuscle invasive bladder cancer in humans. Clinical validation studies will support the potential of this strategy as a complementary solution in clinical practice to reduce the risk of residual bladder cancer disease.

Competing interest statement: F.C., A.C., M.A., I.L., E.A., M. Maturi, E.L., and M.C.F. are inventors of patents regarding GNRs functionalized with peptide Iso4.

This article is a PNAS Direct Submission. G.S. is a guest editor invited by the Editorial Board.

Copyright © 2024 the Author(s). Published by PNAS. This open access article is distributed under [Creative Commons Attribution-NonCommercial-NoDerivatives License 4.0 \(CC BY-NC-ND\)](https://creativecommons.org/licenses/by-nc-nd/4.0/).

¹P.A. and I.L. contributed equally to this work.

²To whom correspondence may be addressed. Email: mauro.comesfranchini@unibo.it, ooi.ean.hin@monash.edu, luca.menichetti@ifc.cnr.it, or alfano.massimo@hsr.it.

This article contains supporting information online at <https://www.pnas.org/lookup/suppl/doi:10.1073/pnas.2411583121/-/DCSupplemental>.

Published September 5, 2024.

microultrasound, which can only detect tumors larger than 5 mm (13, 14). Even cystoscopy, which may include photodynamic diagnosis, has limited diagnostic utility in terms of bladder CIS detection. During cystoscopy and TURBT, numerous biopsies are usually taken from the suspicious urothelium to aid detection and diagnosis (15). Second, residual NMIBC are often chemoresistant, with intravesical instillation of adjuvant therapy failing in approximately 50% of patients (3).

We recently characterized a preclinical model of BC expressing integrin $\alpha 5 \beta 1$, which is also expressed in 75% of the human bladder CIS (16). Using this approach, we delivered a solution to detect BC lesions smaller than 1 mm (16). This solution involves intravesical instillation of urine-stable targeted gold nanorods (GNRs) against integrin $\alpha 5 \beta 1$ to detect BC expressing the same integrin. This was achieved by exploiting the photoacoustic properties of GNRs using photoacoustic (PA) imaging, a diagnostic imaging modality that provides spatial resolution in the range of 50 to 100 microns (17). PA imaging of GNRs is achieved through nanopulsed laser irradiation; however, their irradiation using continuous laser allows the conversion of optical energy to heat and thus their application as photothermal therapy (PTT) (18, 19).

The unique PA and photothermal properties of the GNRs when irradiated with different types of lasers suggested the possibility of an effective BC management strategy that simultaneously detects and treats the lesion.

This study aimed to demonstrate the feasibility of a solution to better manage residual NMIBC. To achieve this aim, we investigated the use of GNRs coated with the biopolymer chitosan (GNRs@Chit) engineered with peptide *Iso4* (head-to-tail cyclized c(CpghisoDGRG), selective for the $\alpha 5 \beta 1$ integrin) (16, 20), to provide simultaneous detection (via PA imaging) and treatment (via GNR-assisted PTT) of BC lesions smaller than 1 millimeter expressing integrin $\alpha 5 \beta 1$.

To gain a mechanistic understanding of the heat transfer process that occurs during PTT, a computational model was developed and validated against a preclinical model of orthotopic BC that expressed the integrin $\alpha 5 \beta 1$. Using a large cohort of clinical specimens, this study confirmed the expression of integrin $\alpha 5 \beta 1$ on bladder CIS, as well as on high-grade pTa and pT1 as diagnosed at TURBT. This study demonstrates the efficacy and safety of GNRs engineered with Chit and *Iso4*, hereafter referred to as GNRs@Chit-*Iso4*, in inducing coagulative necrosis of BC expressing integrin $\alpha 5 \beta 1$. Likewise, current findings show that GNRs@Chit-*Iso4* is feasible for theranostic application for residual BC represented by lesions smaller than 1 mm.

Results

The $\alpha 5 \beta 1$ Integrin Is Expressed by Neoplastic Cells in the NMIBC.

We previously reported that the $\alpha 5 \beta 1$ integrin is expressed by the orthotopic tumor in the MB49-derived preclinical model and in six out of eight (75%) samples of patients diagnosed with CIS (16). In this study, we implemented this information by carrying out the analysis of an extended number of CIS and included specimens from high-grade (HG) NMIBC staged pTa and pT1, for a total of 43 BC specimens and 4 nontumoral bladder specimens.

In the nontumoral tissues, the $\alpha 5$ subunit was not expressed by the urothelial and umbrella cells present in the urothelium but was only expressed by the stromal cells present in the lamina propria (Fig. 1A). The same expression pattern was observed in a clinical specimen of chronic reactive urothelium following radiotherapy (Fig. 1B), characterized by irregular polarization of the nuclei of urothelial cells, hyperplastic umbrella cells, and inflammation in the lamina propria. In the NMIBC specimens, the membranous

expression of the $\alpha 5$ subunit was also identified in the CIS cancer cells ($n = 18/25$ cases, 72%) (Fig. 1C), including CIS that colonized the prostate ducts (Fig. 1D), and HG pTa ($n = 10/11$ cases, 91%) (Fig. 1E). In HG pT1, the $\alpha 5$ subunit was expressed only in the noninvasive region of the neoplasia (Fig. 1F), but not expressed when tumor cells invaded the lamina propria ($n = 7$, 100%) (Fig. 1G). The $\beta 1$ subunit was expressed by urothelial, stromal and tumor cells, as recently reported (16) (data not shown). The outcome of this analysis shows that non-neoplastic urothelial cells were negative for the expression of $\alpha 5 \beta 1$ integrin and that 81% (35 out of 43 cases) of HG NMIBC in the urothelial layer express $\alpha 5 \beta 1$ integrin (Fig. 1H). Overall, these data suggest that the expression of $\alpha 5 \beta 1$ integrin is specific to the neoplastic transformation of urothelial cells when HG neoplasia is in the urothelial layer but is not associated with chronic inflammation.

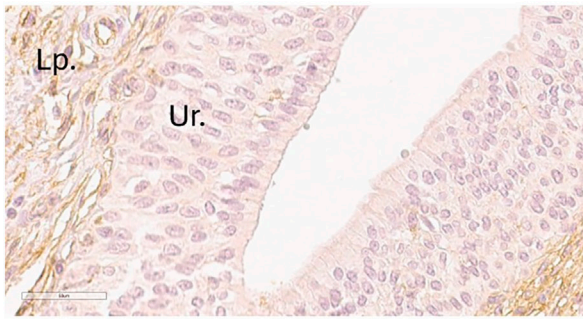
Furthermore, the width of bladder CIS was in the range of 0.15 to 1.2 mm, and the depth was between 10 and 300 μm for single-cell layer or hyperplastic neoplasia, respectively. The width of the pTaG3 and the noninvasive region of pT1G3 was in the range of 1.5 to 5.6 mm, and the depth was between 130 and 900 μm .

GNR-Assisted PTT Induced Coagulative Necrosis of BC. The specificity of GNRs@Chit-*Iso4* (SI Appendix, Fig. S1) to induce GNR-assisted PTT for neoplastic tissue was assessed in a preclinical model represented by mice bearing the MB49-Luc derived orthotopic tumor that expresses integrin $\alpha 5 \beta 1$ (16). Pulsed laser light at 808 nm irradiated from the surface of the abdomen was used to image the specific PA signal of GNRs@Chit-*Iso4*, which is located only at the surface of the tumor mass but not in the urothelium surrounding the neoplasia (Fig. 2A). A preliminary study based on a trial-and-error approach was carried out to identify parameters for laser irradiation that would induce the death of tumor cells bound to GNRs@Chit-*Iso4* but avoid thermal damage to the skin and the surrounding bladder, a consequence that could compromise the survival of the irradiated preclinical model and introduce bias in the estimated efficacy of GNR-assisted PTT. Results of this preliminary study suggest that 3 min of irradiation with continuous laser at 808 nm and a laser power density of 2.54 W/cm^2 at the surface of the abdomen was sufficient to raise the tumor temperature to induce cell death but caused only a 1 to 2 $^{\circ}\text{C}$ increase on the skin surface. Histological analysis of the explanted organ (Fig. 2B) showed no signs of damage in the non-neoplastic tissue near the tumor mass (Fig. 2C) and in the bladder wall penetrated by the laser light (Fig. 2D). We observed signs of coagulative necrosis in the upper part of the neoplastic mass covered with the GNRs@Chit-*Iso4*, a process that occurs in the temperature range of 42 to 46 $^{\circ}\text{C}$ (21), with signs of pyknosis deeper into the neoplastic mass (Fig. 2E). The depth of thermal damage in the tumor mass induced by GNR-assisted PTT was between 500 and 1,300 μm among the different tumors treated, and composed of necrosis and pyknosis, to which pyknosis depth contributed to $31 \pm 4\%$ of the total thermal damage (Fig. 2F).

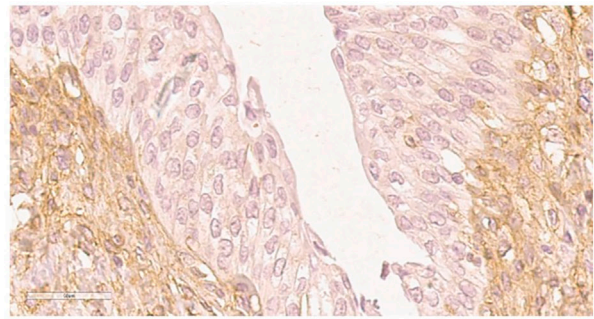
Gradient of Power Density at the Upper and Lower Side of the Bladder.

Tumors may grow at different locations on the bladder surface. Because the bladder is shaped like a hollow ellipsoid and the laser beam follows a Gaussian distribution, the power densities at the upper and lower halves of the bladder may be different. Since our target were small and flat lesions, we estimated the laser power density at the skin surface and at the bottom of the bladder, but not at the tumor surface. Estimation was performed only for control animals without tumors. Results indicated that the power density at the skin surface and bottom surface of the

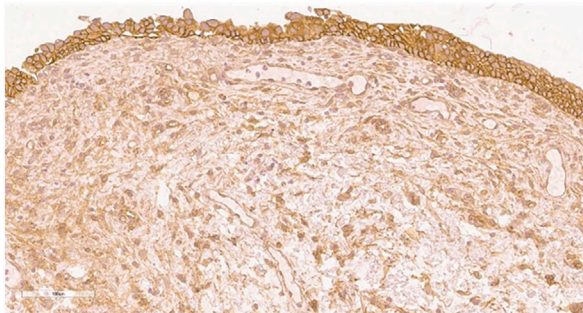
A Non-neoplastic human bladder



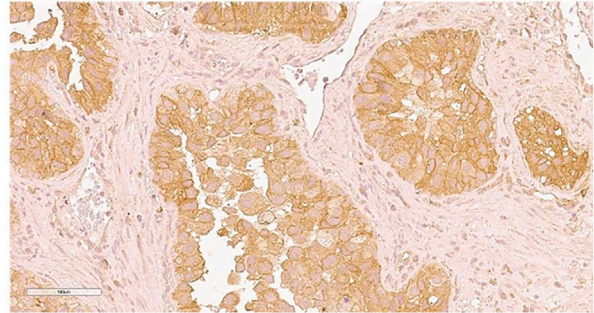
B Chronic reactive urothelium



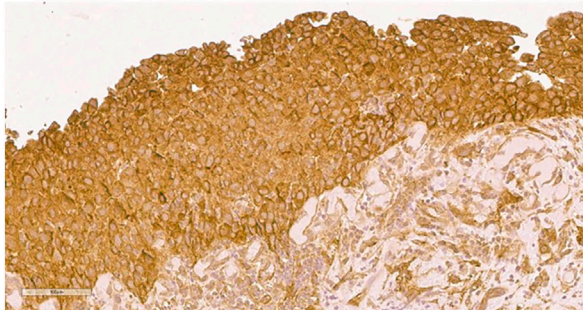
C Human bladder CIS



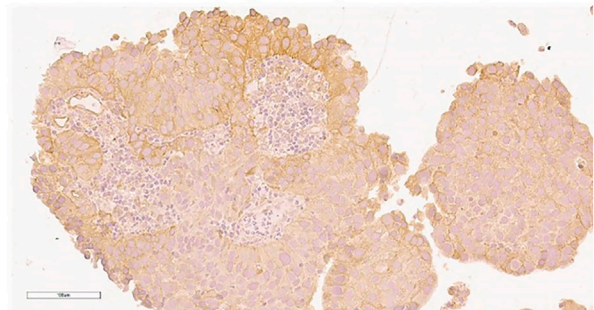
D Urothelial CIS in prostate duct



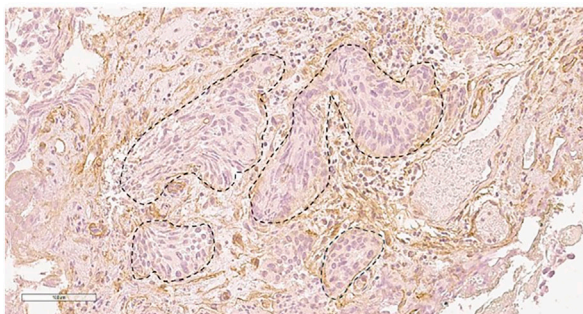
E Human bladder pTaG3



F Human bladder pT1G3 (no invasion)



G Human bladder pT1G3 (invasion)



H

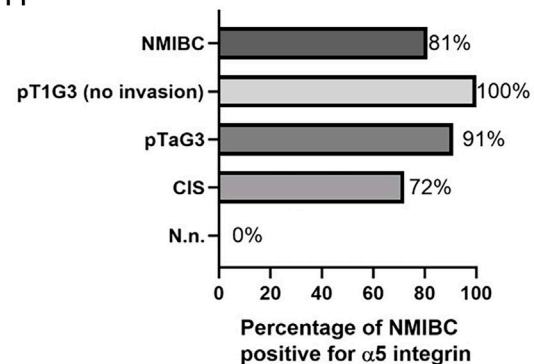


Fig. 1. Expression of the $\alpha 5$ integrin subunit in human NMIBC. Representative immunohistochemistry photomicrographs of human bladder sections of non-neoplastic tissue (A and B), CIS (C and D), HG pTa (pTaG3, E), and HG pT1 (pT1G3) in the urothelial layer (F) and in the lamina propria (G, representative tumor area highlighted by dashed circle); all tissues were obtained by TURB. [Scale bar, (A and B), 50 μ m; (C–G), 100 μ m.] Ur, urothelium, Lp, lamina propria. Quantification of tissues with cells positive for the membranous expression of the $\alpha 5$ subunit and located in the urothelial layer (H); N.n.= non-neoplastic tissue.

bladder was 2.54 and 0.664 W/cm², respectively, which for a 3 min irradiation corresponded to a total energy delivered to the skin and lower bladder surfaces of 120 J and 88 J, respectively (Fig. 2G and *SI Appendix*, Table S1).

GNRs@Chit-Iso4 Mediated the Increase in Temperature and Heat. To associate the necrosis observed from the histological analysis with GNR-assisted PTT, we established the temperature and amount of heat generated during laser irradiation. After

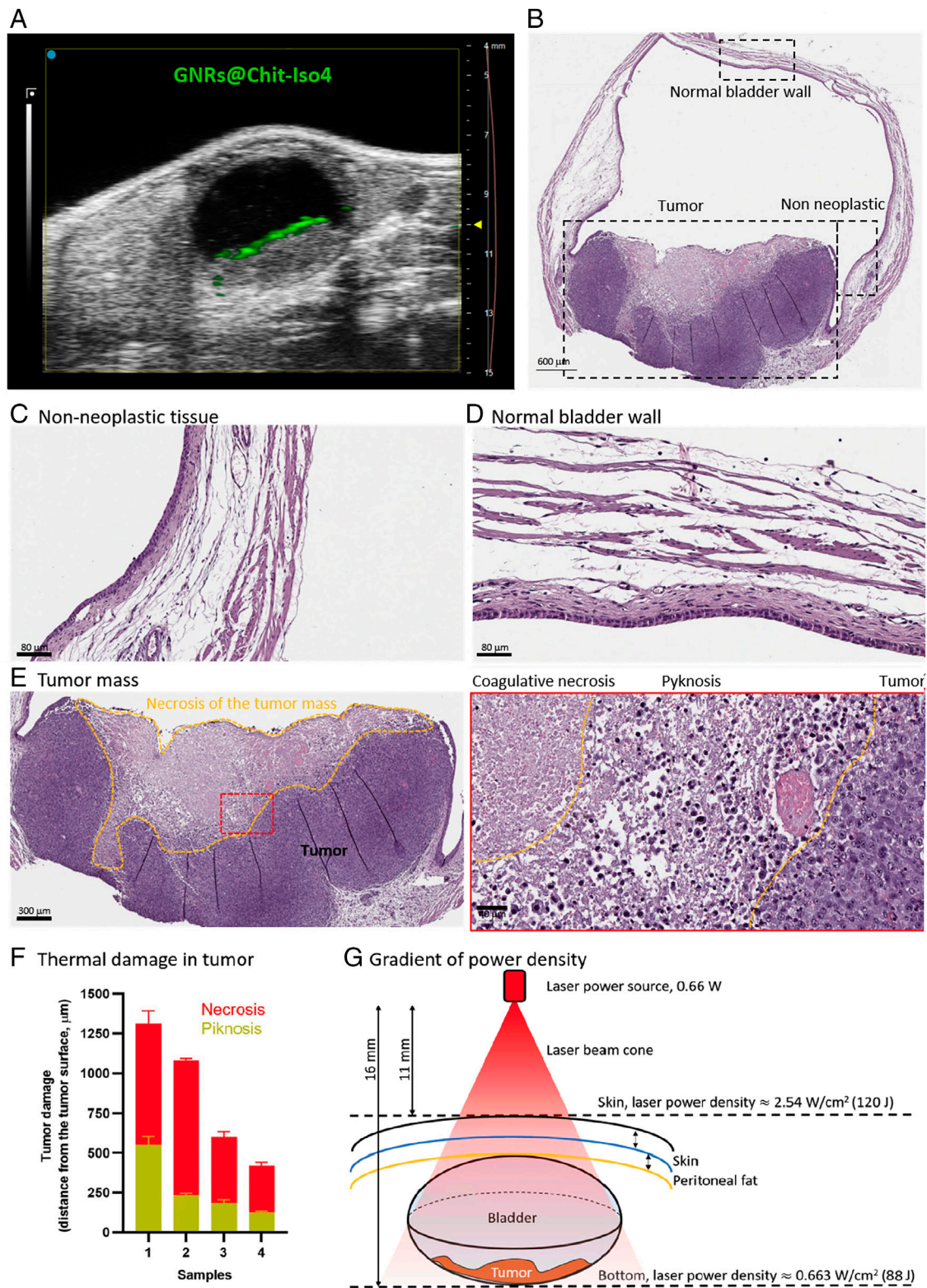


Fig. 2. Theranostic application of GNRs@Chit-Iso4 against the murine MB49-Luc orthotopic bladder tumor. (A) Axial frame of the murine bladder with a tumor detected by ultrasound imaging and specific photoacoustic imaging of GNRs@Chit-Iso4 obtained after spectral unmixing using the reference photoacoustic spectra of melanin, deoxygenated and oxygenated blood (after intravesical instillation of 10 nmol Au; 100 μL of 100 μM GNRs@Chit-Iso4): one representative frame taken in the middle of the bladder, with the time gain compensation (TGC) shown at the right side of the image. (B) Hematoxylin-eosin stain of the tissue section from the same animal shown in panel A, after 3 min of irradiation with continuous laser at a laser power density of 0.664 W/cm². (C) The non-neoplastic tissue near the necrotic tumor mass. (D) The normal bladder wall that was passed through by the laser. (E) The tumor mass with the necrotic area highlighted by the yellow dashed border, followed by a magnification of the region within the red dotted frame showing the coagulative necrosis characterized by the absence of cell nuclei, and the pyknosis characterized by the condensation of chromatin in the nuclei of the cells. (F) Quantification of the thermal damage in the neoplastic tissue, estimated as necrosis and pyknosis from the tumor surface to the inner part of the mass (measurements on 6 hematoxylin/eosin slides each tumor, four tumors from four different animals). (G) Scheme and parameters used to establish the gradient of laser power density at the upper and lower side of the bladder; bladder dimensions and distance from the skin were obtained from US images of the mouse in the supine position. Data shown in panels A–F are from one representative animal out of three tested. Data shown in panel F were from eight ex vivo murine bladders.

demonstrating the *in vivo* binding of GNRs@Chit-Iso4 to the luminal area of the bladder tumor (*SI Appendix, Fig. S2*), laser irradiation and measurement of temperature rise were performed *ex vivo*. To ensure that the measurement of bladder temperature rise during laser irradiation was not biased by heat absorption in the surrounding organs, the bladder from the treated mice was removed together with the layer of tissue surrounding the bladder and the skin. The optical fiber for laser irradiation was placed above the skin, and the NIR thermal camera was placed under the bladder (*SI Appendix, Fig. S3*).

Three minutes of laser irradiation of the tumor-bearing bladder (without GNRs@Chit-Iso4) and the healthy bladder (without tumor) induced a temperature increase of 2.54 ± 0.52 °C across the bottom surface of the bladder, without difference between the two groups. Conversely, a significant increase in temperature of 5.36 ± 1.25 °C was observed for the tumor bounded with GNRs@Chit-Iso4 (*Fig. 3A*). Likewise, significant heat sustainment mediated by irradiation of GNRs was recorded in the 4 min following laser shutdown (*Fig. 3B*).

Density of Gold on the BC Luminal Area. To establish the relationship between the bladder tumor area, the amount of gold bound to the tumor, and the maximum temperature rise, we used data from animals with different tumor sizes after intravesical instillation of GNRs@Chit-Iso4 (*SI Appendix, Fig. S2 and Table S2*). The maximum temperature increase was proportional to the total amount of gold bound to the tumor surface, as recently reported (22), and the total amount of gold and the maximum temperature increase were proportional to the tumor area exposed to the bladder lumen (*Fig. 3C*).

Of the GNRs that were intravesically instilled, the median amount of gold recovered from the surface of the tumor was 10%, ranging from 3% to 22% according to the tumor area (*Fig. 3D*). Indeed, the density of gold on the neoplastic tissue was not dependent on the tumor size, with a median density of gold of 7.5 ng/mm² of neoplastic tissue, ranging from 6 to 8 ng/mm² and one outlier at 17 ng/mm² (*Fig. 3E*). According to the GNR dimension of the GNRs that we used (16), we estimated that 7.5 ng/mm² corresponds to 22 million GNRs/mm².

Efficacy and Specificity of GNR-Assisted PTT in Reducing Tumor Mass. To assess the efficacy and specificity of GNR-assisted PTT in reducing tumor mass, mice were randomized according to the bioluminescence signal of the tumor mass. Three groups of mice with similar tumor masses were used (*Fig. 3F*). The parameters used for *in vivo* GNR-assisted PTT were as follows: i) laser wavelength of 808 nm, ii) laser power density on the skin of 2.4 W/cm² (laser power 0.66 W and effective illumination area defined by a radius of 5.75 mm), and iii) laser probe placed 11 mm from the skin. Irradiation for 3 and 5 min did not reduce the tumor mass, as indicated by the absence of a reduction in the bioluminescence signal. After intravesical instillation of GNRs@Chit-Iso4, a significant reduction in the tumor mass was found, with no difference between 3 and 5 min of irradiation (*Fig. 3F*). The specificity of the targeted GNR-assisted PTT was further demonstrated using the murine BC cell line MB49-Luc, whose viability was significantly reduced only after treatment with GNRs@Chit-Iso4 and irradiated (*Fig. 3G*).

Estimation of Temperature Rise at the Tumor Surface. Although the findings reported in “GNRs@Chit-Iso4 mediated the increase in temperature and heat” showed a significant increase in temperature in the presence of GNRs@Chit-Iso4, this information is biased by the measurement of temperature at the exterior

surface of the bladder wall, the absorption of heat by the bladder wall, the tissue/fat surrounding the bladder, and the convective dispersion of heat by the urine. To estimate the temperature rise across the tumor surface, we developed a computational model that approximated the conditions of the *ex vivo* experiments, such as the amount of gold bound to the tumor, as determined experimentally (*SI Appendix, Table S2*), and tumor surface area exposed to the bladder lumen (*SI Appendix, Table S3*). The thermal effects of small and large tumors can be distinguished by analyzing the temperature rise across the tumor surface. The temperature rise at the top surface of the tumor where GNR attachment was expected was found to range from 9 to 23 °C for tumors with small (3.82 mm²) and large (69.58 mm²) surface areas, respectively (*Fig. 4A and SI Appendix, Table S4*). In the absence of GNRs, the range of temperature rise was narrower, between 5 and 7 °C (*SI Appendix, Table S4*). When we considered the bottom surface of the tumor, the temperature rise mediated by the GNRs ranged from 7 to 19 °C for tumors with small (3.82 mm²) and large (69.58 mm²) surface areas, respectively (*Fig. 4A*). In the absence of the GNRs, the temperature rise was very similar to that estimated on the surface of the tumor (*SI Appendix, Table S4*). These findings indicate that the temperature rise in the presence of GNRs was dependent on the amount of GNRs bound to the tumor surface, and in the absence of GNRs, it was mediated by the absorption of photons by the tumor mass. Furthermore, the information presented provides insight into the variable distance of thermal damage observed in different tumors, with larger tumors having a greater surface area for the attachment of GNRs, and hence, can generate more heat that spreads deeper into the tissue (as previously reported in *Fig. 1F*).

Computational Model for GNRs@Chit-Iso4-Assisted PTT of Small BC Lesions. Having established the feasibility and specificity of PTT assisted by GNRs@Chit-Iso4 for tumors expressing integrin $\alpha 5\beta 1$, we carried out simulations to test the hypothesis of a localized thermal effect driven by GNRs. A dedicated heat transfer model for small BC lesions was developed. The model considered a bladder tumor resembling a cylinder with a radius of 0.5 mm (i.e., width of 1.0 mm) and thickness of 0.2 mm, with an estimated volume of 0.192 mm³. GNRs@Chit-Iso4 is assumed to bind to the luminal side after intravesical instillation. The model assumed that the mouse was in the supine position, and the bladder was irradiated from the top using a 0.66 W continuous laser with a beam radius of 10 mm evaluated at full-width half maximum (*Fig. 4B*). The amount of GNRs distributed across the tumor surface was estimated based on the GNR attachment density, 7.5 ng/mm² determined experimentally (as previously reported in *Fig. 3E*).

In the model, the average tumor temperature was 43.0 °C, while on the skin surface, the maximum temperature was 46.6 °C after 3 min of irradiation (*Fig. 4C*). Note that the tumor temperature was almost homogeneous (average vs. maximum of 43.0 vs. 43.3 °C). When the irradiation duration was increased to 5 min, the average tumor temperature increased to 45.7 °C, whereas on the skin surface, the maximum temperature was 48.9 °C (*Fig. 4D*). Although prolonging the laser exposure helped to elevate the tumor temperature, it also increased the temperature on the skin surface to increase. Nevertheless, it is noteworthy that the maximum temperature on the skin at 46.6 °C after 3 min occurred only across a very small region (width < 1 mm) immediately above the tumor. As observed from the temperature contours (*Fig. 4C*), most of the skin surface is still below 40 °C.

The absence of significant thermal damage to bladder tissue is also evident in *Fig. 4E*. The green curve represents the 42 °C

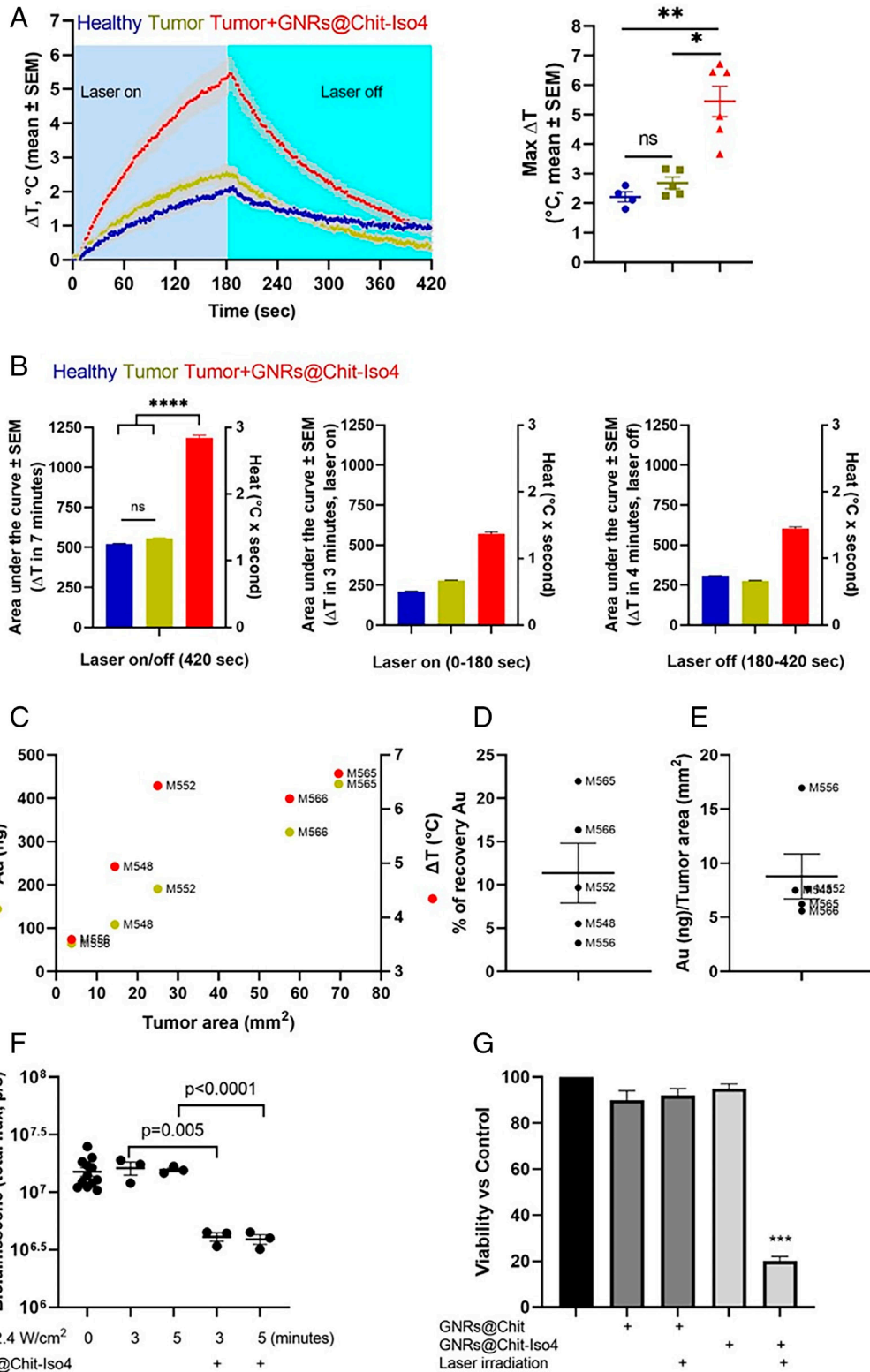


Fig. 3. The specificity of thermal therapy mediated by GNRs@Chit-Iso4 against bladder cancer cells expressing the integrin $\alpha 5\beta 1$. Intravesical instillation of 1,970 ng of Au (100 μL of 100 μM of GNRs@Chit-Iso4) was performed in five animals with bladder orthotopic tumors of different sizes: after 15 min of incubation followed by three intravesical washes with saline solution, the binding of GNRs@Chit-Iso4 to the tumor area was visualized by PAUS imaging (SI Appendix, Fig. S7). (A) *Left*: Kinetic of temperature rise during laser irradiation and temperature fall during the laser off period; *Right*: maximum of temperature rise measured after 180 s of laser irradiation; each symbol in the dot plot represents a single animal. (B) The total temperature and heat calculated during the i) laser on/off period, ii) on period, and iii) off period. (C) Quantification of gold and maximum of the measured temperature rise according to the luminal area of the bladder tumor. (D) Recovery of gold. (E) Density of gold on neoplastic tissue. Each dot represents a single animal, with raw data reported in SI Appendix, Table S2. Lines and bars in panels B and C show means and SEM. (F) Tumor bioluminescence before and after laser irradiation (3 and 5 min) in the absence and presence of GNRs@Chit-Iso4 (intravesical instillation of 10 nmol Au, 100 μL of 100 μM of GNRs@Chit-Iso4); each symbol represents one animal before and after laser irradiation of the bladder, tested 9 to 12 d after the intravesical instillation of the MB49-Luc cells (statistical significance by the paired *t* test is shown by asterisks). (G) Cell viability of MB49-Luc cells cultivated *in vitro* was established 16 h after treatment with GNRs@Chit or GNRs@Chit-Iso4 and left not irradiated or irradiated with a 808 nm continuous laser. The experiment was performed in quadruplicate, and data are expressed as mean \pm SEM.

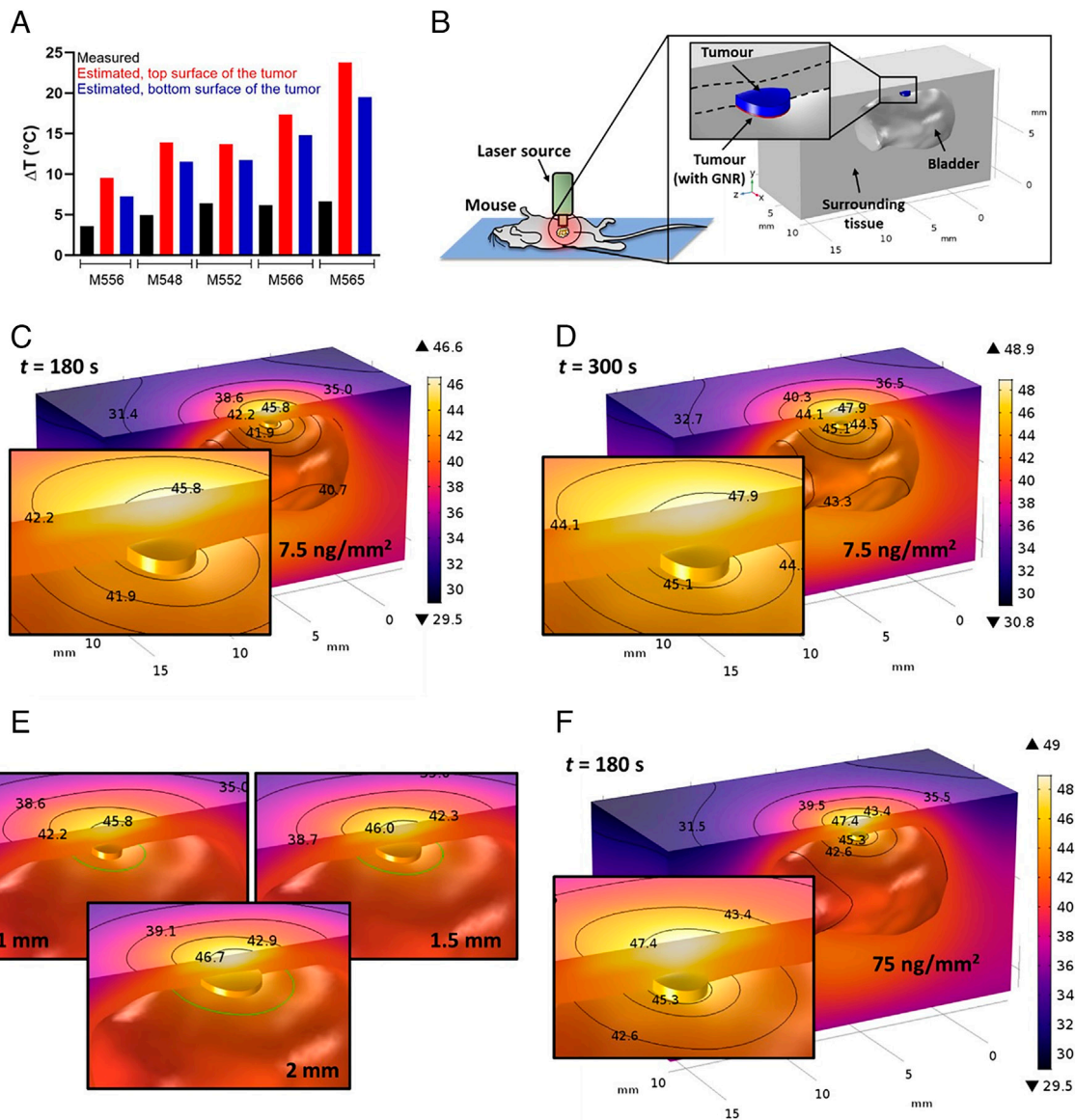


Fig. 4. Computational model for GNRs@Chit-iso4-assisted PTT of ex vivo bladder and small bladder cancer lesions. (A) Comparison of temperature rise across the top and bottom surfaces of the tumor estimated from the model of ex vivo bladder. (B) Schematic of the computational model representing the region of interest during GNR-assisted PTT of bladder cancer in the mouse. The blue region represents the tumor, while the thin region in red represents the layer of the tumor with GNR attachment. The position of the laser probe in contact with the skin is also shown. (C) Contours of temperature after 180 s of laser irradiation at a laser power of 0.66 W in the model that considers an Au density of 7.5 ng/mm² at the tumor surface (the *Inset* shows an enlarged view of the temperature contours across the tumor). (D) As in panel B, but considering 300 s of irradiation, with the temperature scale capped at 48.9 °C for better visualization (the *Inset* shows enlarged views of the temperature contours across the tumor). (E) Spread of the 42 °C isotherm (green) from the tumor boundary for cases with tumor radii of 1, 1.5, and 2 mm. (F) As in panel B but considering a 10-fold higher Au density (75 ng/mm²) of the tumor surface (the *Inset* shows an enlarged view of the temperature contours across the tumor).

isotherm, where the spread to 1 mm from the tumor boundary suggests that heat propagation in the lateral direction is confined to a small region around the tumor. This appeared to be independent of the tumor size, as simulations repeated for tumor radius of 1.5 and 2 mm showed that the 42 °C isotherm did not extend beyond 1 to 2 mm from the tumor boundary.

We also considered a hypothetical case in which there was a 10-fold increase in GNR attachment to the tumor surface (i.e., 75 ng/mm²). When the GNR concentration was increased by 10×, the average tumor temperature after 3 min of irradiation was 47.1 °C, while the maximum temperature on the skin surface was 49.9 °C (Fig. 4F), a temperature known to induce burns on mouse skin (23).

The results obtained from this simulation study are in agreement with the setup identified in our preliminary study using the trial-and-error method (see “GNR-assisted PTT induced coagulative necrosis of BC”), where 3 min of irradiation-induced

coagulative necrosis of the tumor that was covered with GNRs, in the absence of damage to the skin surface and the bladder (Fig. 2).

Early Detection of BC Lesions. Using the clearly visible tumors reported above, we demonstrated the feasibility and specificity of GNR-assisted PTT for BC therapy. Furthermore, the computational model shows that GNR-assisted PTT can be achieved for smaller tumors, such as CIS. Therefore, studies were repeated using the preclinical model in the time frame in which the tumor mass was not yet visible. Here, we report that several neoplastic lesions smaller than 0.5 mm and undetectable by high-resolution US were recognized through PA imaging of GNRs@Chit-Iso4 (Fig. 5A). In the following days, the small neoplastic lesions developed into neoplastic masses that coalesced to form a large irregular tumor (Fig. 5B), with the tumor growing into the bladder lumen and the tumor cells infiltrating the lamina propria

(Fig. 5C). The biology of the tumor onset and progression reported here is in agreement with a previous report (24) which shows that this preclinical model is characterized by the early establishment of clusters of a few MB49 cells attached to the luminal side of the urothelium, followed by the onset of sessile carcinoma that develops toward the bladder lumen, and pedunculated tumors that also infiltrate the lamina propria (24).

GNRs@Chit-Iso4-Assisted PTT Reduced Tumor Growth and the Number of Small Neoplastic Areas. We evaluated the efficacy of GNR-assisted PTT in reducing tumor growth over 28 d of follow-up. In this framework, mice were instilled with MB49-Luc cells and randomized on day 9 according to the bioluminescence signal of the tumor to receive or not receive GNRs@Chit-Iso4-assisted PTT (Fig. 6A). Randomization was performed such that animals with low/middle and high bioluminescence signals ($<10^6$, $>10^6$ total flux, p/s) were present in both experimental groups (Fig. 6B). Survival analysis showed a more prolonged survival of mice treated with GNR-assisted PTT than that of the untreated group (Fig. 6C).

In this preclinical model, tumor progression was rapid (Fig. 6D), leading to bladder obstruction that contributed to the death of the animals. In the context of PA imaging of GNRs@Chit-Iso4 and GNR-assisted PTT, we highlight two scenarios: i) the presence of tumor lesions detectable by US and PA imaging of GNRs@Chit-Iso4, and ii) tumor lesions smaller than 0.5 mm and only detectable by PA imaging of GNRs@Chit-Iso4. In animals with tumor lesions that were detectable by both US and PA imaging of GNRs@Chit-Iso4, GNR-assisted PTT successfully reduced the tumor growth (Fig. 6E). In animals in which tumor lesions were detected only by PA imaging of GNRs@Chit-Iso4, we identified several lesions with diameters smaller than 0.5 mm in the entire bladder volume (Fig. 6F), which is in agreement with the presence of clusters of few MB49 cells attached to the urothelium at earlier times after intravesical instillation (24). After GNR-assisted PTT, only one tumor region was identified, with a significantly smaller tumor volume than that without GNR-assisted PTT (Fig. 6F).

Discussion

We established a strategy for the simultaneous detection and treatment via hyperthermia of BC lesions through specific targeting by using GNRs@Chit engineered with the peptide Iso4 (GNRs@Chit-Iso4) to specifically recognize integrin $\alpha 5 \beta 1$, which is present in 81% of HG NMIBC. GNRs@Chit-Iso4-induced PTT improved the survival of the treated mice by effectively reducing the tumor mass through cell necrosis. This solution also emerged to be safe, as both *in vivo* data and computational modeling demonstrated the absence of thermal damage to the surrounding non-neoplastic tissue, the maximum distance reached from the therapeutic temperature ($>42^\circ\text{C}$) from the boundary of the tumor was estimated at 1 mm.

The results from our heat transfer simulations demonstrated the ability of the GNRs to absorb photons efficiently and convert optical energy to heat. The heat is generated around the tumor surface where GNRs bind to then spreads to other regions either by conduction through the tissues or by convection via urine flow (SI Appendix, Fig. S4B). We acknowledge an overestimation of the temperatures at the bottom surface of the bladder compared with the experiments (SI Appendix, Table S4). This may be explained by the loss of photons during the experiments as the laser propagated through different tissue layers of the excised bladder. Simulations carried out on the model with bladder CIS also

demonstrated the hyperthermic capability of the GNRs, although the heating intensity was somewhat reduced because of the small surface area of the submillimeter tumor, which reduces the amount of GNRs that can bind to the tumor. Even so, the *in vivo* study demonstrated that the heat generated within the submillimeter tumor was sufficient to induce necrosis in few tumor cells present in the lesion, further demonstrating the efficacy of the GNR-assisted PTT setup.

The necrosis induced by GNR-assisted PTT has threefold added value, namely i) not being influenced by the chemoresistance phenomenon; ii) being equally effective in men, women, and frail individuals; and iii) being able to induce the recruitment of immune cells that could eliminate residual tumor cells (25, 26).

Through the intravesical instillation of GNRs@Chit-Iso4 and by means of the associated PA imaging and the PTT effect, we have demonstrated the possibility of estimating the density of gold per squared millimeter attached to neoplastic tissue exposed to the luminal side of the bladder that upon laser irradiation, was sufficient to provide a significant increase in total heat absorption and temperature rise.

This solution was designed according to clinical procedures for NMIBC detection (i.e., bladder lavage and tumor detection by cystoscopy), was designed not to change the clinical approach and to be completed in approximately 20 min. Furthermore, using GNRs that can release US and heat upon irradiation with a pulsed and continuous laser at 808 nm offers the advantage of utilizing a single optical fiber. This approach is also safe as the 808 nm wavelength is in the biological optical window (near infrared at a wavelength of 680 to 970 nm), which is approved for clinical practice by the American National Standards Institute (27). Overall, this solution offers unmet theranostic opportunities and, as it is unrelated to cellular metabolism, can overcome bias in gender medicine (28), being equally effective in male and female BC patients (29, 30). Likewise, this solution is also suitable for frail patients who may have troubles in tolerating the standard care for bladder CIS, i.e., the intravesical instillation of Bacillus Calmette–Guerin (31).

The feasibility of intravesical instillation of GNRs to deliver PTT against BC has been previously demonstrated. Reduced tumor growth was achieved in the orthotopic mouse xenograft model with the human BC cells T24 upon i) EGFR-targeted GNRs left in the bladder for 2 h, for six weekly intravesical instillation and PTT obtained with 808 nm laser and laser power density of 2.1 W/cm^2 (32), or ii) intravesical instillation of Au@Chl/Fe-CPBA nanorods and irradiation with 785 nm laser and laser power density of 1 W/cm^2 (33). A reduction in MB49-induced murine orthotopic BC growth has also been reported with other forms of nanoparticles, such as targeted carbon nanotubes irradiated with a laser wavelength of 980 nm and a power density of 1.7 W/cm^2 for a total energy density of 50 J/cm^2 (34). Our solution overcomes the limitations identified in the above studies, such as the 2-h incubation of GNRs in the bladder and six weekly instillations. In addition to PTT, our proposed solution can simultaneously visualize smaller lesions using the same nanoparticles and laser wavelengths via PA imaging.

The present study is not devoid of limitations. First, in this preclinical model, MB49-Luc cells that bind to the urothelium give rise to sessile and pedunculated tumors (24). Therefore, PTT induced after intravesical instillation of GNRs@Chit-Iso4 efficiently reduced the tumor mass in the murine bladder lumen, but the effect did not reach the tumor cells in the lamina propria. As a result, this study could not demonstrate the curative application of GNR-assisted PTT, as also reported in the studies above (32–34).

Days after intravesical instillation of the murine bladder cancer cells MB49-Luc

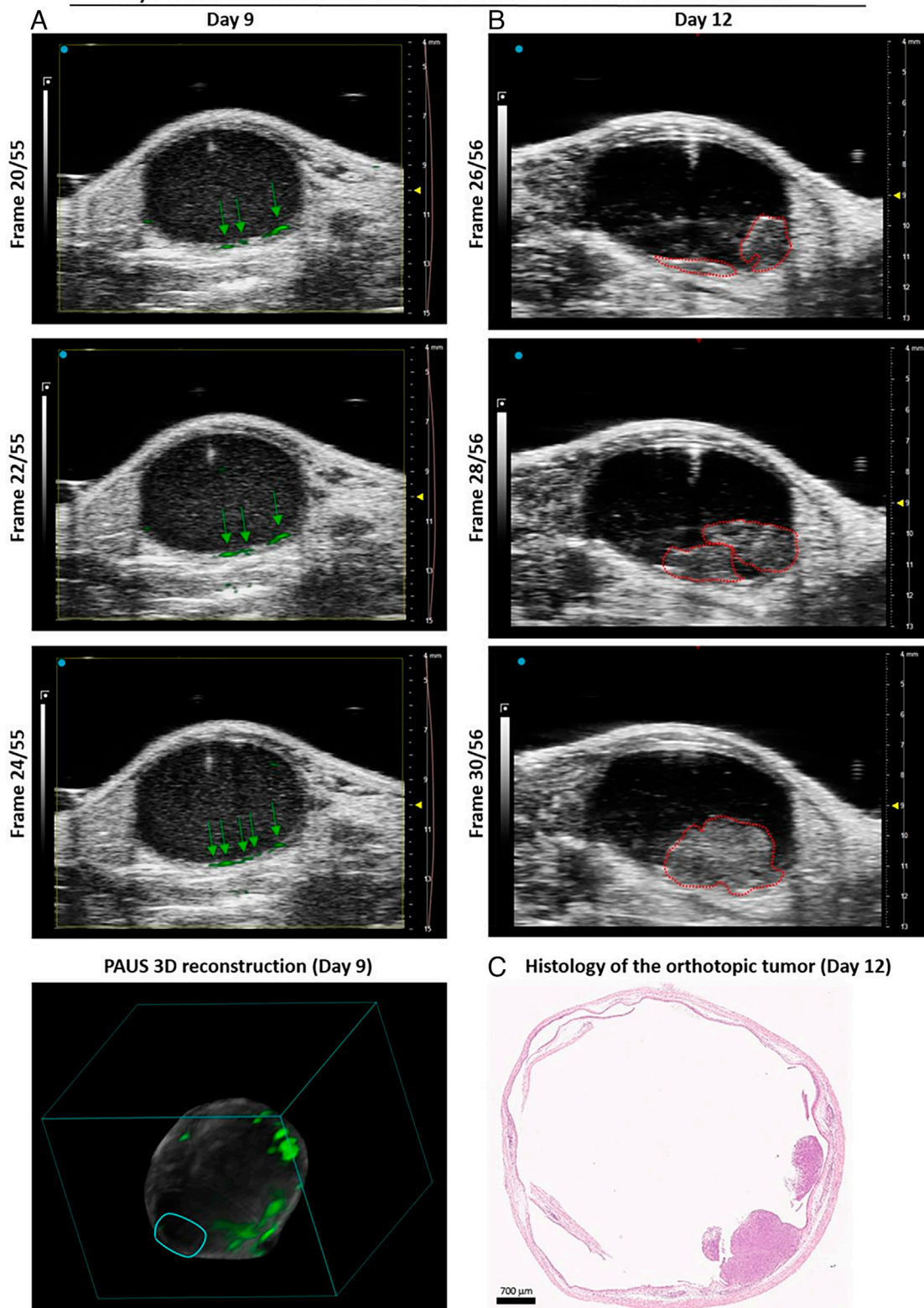


Fig. 5. PA imaging of GNRs@Chit-Iso4 allows the identification of small neoplastic lesions, which rapidly merge to give rise to neoplastic mass with big volume and irregular shape. (A) Three representative axial frames of US imaging of a murine bladder 9 d after the intravesical instillation of murine bladder cancer cells MB49-Luc from the scanning of the entire bladder volume, with neoplastic lesions detected only by the PA imaging of GNRs@Chit-Iso4 (intravesical instillation of 10 nmol Au; 100 μ L of 100 μ M of GNRs@Chit-Iso4) indicated by the green arrows, followed by the 3D reconstruction of PA and US imaging. The PA imaging of GNRs@Chit-Iso4 is after unmixing the photoacoustic signal of melanin, deoxy- and oxy-generated blood. (B) US imaging of the bladder from the same animal reported in panel A, 3 d after the detection of the neoplastic lesions by the PA imaging of GNRs@Chit-Iso4: three axial frames showing the presence of two distinct tumor masses (frame 26, red dashed contours) that get in contact (frame 28, red dashed contours) and merge in a single tumor mass with irregular shape (frame 30, red dashed contour). Time gain compensation is shown on the right side of each PAUS and US image. (C) Histology of the orthotopic bladder cancer 12 d after the intravesical instillation of the murine bladder cancer cell line MB49-Luc. Data are representative of the follow-up of one animal out of five.

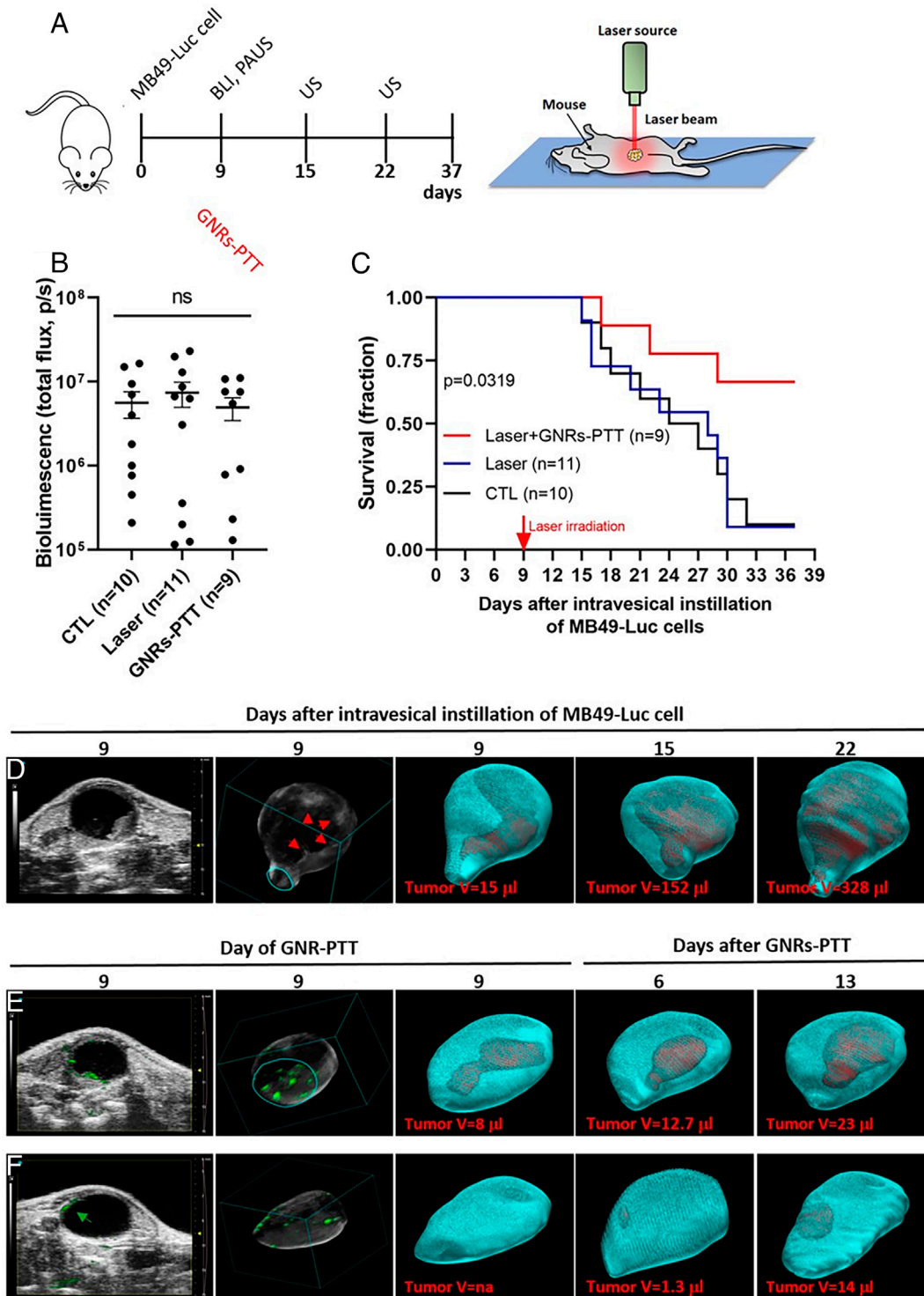


Fig. 6. GNR-assisted PTT of orthotopic bladder cancer improves the survival of the preclinical model. (A) Scheme of the experimental procedure, starting from the intravesical instillation of MB49-Luc cells at day 0, bioluminescence (BLI) quantification, and PAUS imaging at day 9 and then intravesical instillation of GNRs@Chit-Iso4 (100 μ L of 100 μ M of GNRs@Chit-Iso4) followed by GNR-assisted PTT; the tumor growth was evaluated in the two following time points by US imaging, and the mice were euthanized according to the approved procedure by the Institutional Animal Care and Use Committee of San Raffaele Scientific Institute and were performed according to the prescribed guidelines. The cartoon shows the GNR-assisted PTT performed with the laser probe placed 11 mm from the skin. (B) Quantification of bioluminescence of the bladder tumor 9 d after the implantation of the MB49-Luc cells (n.s. = not significant). (C) Survival analysis of animals instilled with the GNRs@Chit-Iso4 (intravesical instillation of 10 nmol Au) and irradiated with a laser power density 0.664 W/cm² for 3 min vs. laser irradiated animals without GNRs vs. control animals (CTL, no GNRs, no laser irradiation); survival analysis was truncated at day 37 after the instillation of murine bladder cancer cells MB49-Luc according to ethical guidelines. Statistical analysis was performed by using the log-rank (Mantel-Cox) test. (D) Axial frame and 3D visualization of US imaging of the murine bladder with tumor (red arrows showing multiple neoplastic mass), followed by the 3D reconstruction of the bladder volume (light blue) and quantification of the tumor volume (red) during the follow up; tumor volume is reported at the bottom of each image. One animal representative of 11. (E) Axial frame and 3D visualization of the murine bladder with tumor recognized by US and PA imaging of GNRs@Chit-Iso4, followed by the 3D reconstruction of the bladder volume and quantification of the tumor volume after GNR-assisted PTT. One animal representative of five. (F) Axial frame and 3D visualization of the murine bladder in which the tumor was not detected by US imaging but in which several neoplastic lesions were identified by the PA imaging of GNRs@Chit-Iso4, followed by the 3D reconstruction of the bladder volume and quantification of the tumor volume after GNR-assisted PTT. One animal representative of four (n.a.; not available).

Second, intravesical insertion of an optical fiber for PTT is not feasible for small animals without damaging the urethra and affecting the survival of the preclinical model. This technological limitation necessitated continuous laser irradiation from outside the abdomen and, therefore, consideration of potential side effects on the skin surface. However, in the clinical setting, the two limitations reported above can be overcome by i) modification of the laser delivery system such as a fiber optic placed inside and guided by a cystoscope, an approach that would allow the tumor to be irradiated directly by using lower laser power to attain the same temperature rise due to minimal photon loss from scattering, and ii) NMIBC is present in the urothelium (35, 36) and exposed to the bladder lumen because of the denudation of the epithelium devoid of umbrella cells when neoplasia is present (37).

Third, regarding tumor biology, the present solution targets integrin $\alpha 5\beta 1$ that is expressed in 81% of HG NMIBC, as similarly reported for other neoplasia of epithelial origin such as ovarian and cervical tumors, in which 80% and 84% of tumors are positive for the expression of integrin $\alpha 5\beta 1$ and significantly correlate with higher clinical stage (38, 39). For the HG NMIBC that expresses the integrin $\alpha 5\beta 1$, the expression is in all the neoplastic cells located in the urothelium. Furthermore, the efficacy of GNR-assisted PTT may extend beyond and below the contact area of the nanoparticles following necrosis-induced recruitment of the immune system (25, 26); this effect might contribute to the control of cancer cells located in the lamina propria that lost the integrin $\alpha 5\beta 1$ as the bladder cancer at stage T1, and contributing to overcome the barrier represented by intratumor heterogeneity. For HG NMIBC that do not express the integrin $\alpha 5\beta 1$, this limitation can be overcome by using an additional target such as cytokeratin 20, expressed in 60% of patients with bladder CIS (40, 41). Therefore, the biological limitations due to tumor heterogeneity between tumors can be solved using the same GNRs targeted to two neoplastic markers or two formulations of GNRs targeted to each marker.

This study demonstrated the feasibility of a solution for GNR-assisted early detection and PTT of small BC lesions expressing integrin $\alpha 5\beta 1$. The feasibility of the solution shown in the preclinical orthotopic BC model that shares features with human NMIBC opens broad avenues for its application in clinical scenarios. The innovative aspect of the theranostic solution provided by the GNRs@Chit-Iso4 against small BC lesions expressing integrin $\alpha 5\beta 1$ offers the possibility to identify and treat the residual HG disease found after the first TURBT (4) and is associated with high or very high risk of relapse and progression (42). Our solution detects and treats bladder lesions that are not visible during TURBT and chemoresistance in most cases and is complementary to TURBT and current therapies for better management and improved clinical outcomes of patients with high-risk or very-high-risk disease, for whom the best treatment is radical cystectomy (43). This solution can be applied to a variety of NMIBC patients, such as i) at the first TURBT to detect the smaller lesions and thus to provide a more accurate diagnosis (i.e., presence of CIS < 1 mm) to drive the follow-up; ii) in a second-look TURBT to identify the residual disease; iii) in relapsing patients where GNR-assisted PTT can be

applied; and iv) to investigate and treat residual disease in patients enrolled in bladder-sparing protocols (44).

Materials and Methods

Detailed information is reported in Supplementary Information, showing materials and detailed methods concerning i) histology and immunohistochemistry analysis, ii) induction of tumor in the preclinical model, iii) protocol for the intravesical instillation of the gold nanoparticles, iv) US and photoacoustic imaging, v) in vitro and in vivo protocols for GNR-assisted PTT, and vi) mathematical modeling.

The study on the human patient cohort was conducted in compliance with the principles of the Declaration of Helsinki, and all patients signed an informed consent agreement to deliver their own anonymous information for future studies. This study was approved by the Institutional Review Board (Ethic Committee IRCCS Ospedale San Raffaele, Milan, Italy; protocol URBBAN). All procedures and studies involving mice were approved by the Institutional Animal Care and Use Committee of San Raffaele Scientific Institute and were performed according to the prescribed guidelines (IACUC, Approval No. 942).

Data, Materials, and Software Availability. The authors confirm that the data supporting the findings of this study are summarized and available within the article and its supplementary material (*SI Appendix, Tables S1 and S2*). The raw data that support the findings of this study are available ([10.17632/bwbsk-2wr3z.1](https://doi.org/10.17632/bwbsk-2wr3z.1)) (45). All other data are included in the manuscript and/or supporting information.

ACKNOWLEDGMENTS. We thank Dr. Antonello Spinelli, Dr. Laura Perani, Dr. Amleto Fiocchi (Preclinical Imaging Facility, Istituto di Ricovero e Cura a Carattere Scientifico Ospedale San Raffaele), and Dr. Rossana Norata (Department of Pathology, IRCCS Ospedale San Raffaele) for their technical support. Murine bioluminescent MB49-Luc cells were kindly provided by Prof. Carla Molthoff (Vrije Universiteit University Medical Center, The Netherlands). This study was funded by the European Union's Horizon 2020 research and innovation program under Grant Agreement No. 801126 and Horizon Europe under Grant Agreement No. 101113193. The funding sources had no role in the design of this study, data interpretation, or writing of the manuscript. The Euro-Bioluminescence research infrastructure located at the National Council of Research in Pisa has enabled open access to imaging technologies in the fields of biological and biomedical imaging, thereby providing support to this study.

Author affiliations: ^aNational Council of Research-Institute of Clinical Physiology, Pisa 56124, Italy; ^bDivision of Experimental Oncology, Urological Research Institute (URI), Istituto di Ricovero e Cura a Carattere Scientifico (IRCCS) Ospedale San Raffaele, Milan 20132, Italy; ^cDepartment of Urology, Istituto di Ricovero e Cura a Carattere Scientifico (IRCCS) San Raffaele Scientific Institute, Milan 20132, Italy; ^dNational Research Council (CNR), Institute of Chemistry of Organometallic Compounds, Pisa 56124, Italy; ^eUniversità Vita-Salute San Raffaele, Milan 20132, Italy; ^fDepartment of Industrial Chemistry, Toso Montanari, University of Bologna, Bologna 40129, Italy; ^gDivision of Experimental Oncology, Tumor Biology and Vascular Targeting Unit, Istituto di Ricovero e Cura a Carattere Scientifico (IRCCS) San Raffaele Scientific Institute, Milan 20132, Italy; ^hDepartment of Pathology, Pathology Unit, Istituto di Ricovero e Cura a Carattere Scientifico (IRCCS) San Raffaele Scientific Institute, Milan 20132, Italy; ⁱAscend Technologies Ltd, Southampton SO15 2BG, Hampshire, United Kingdom; ^jFUJIFILM Visualsonics Inc., Amsterdam AB 1114, The Netherlands; and ^kMedical Engineering and Technology Hub, School of Engineering, Monash University Malaysia, Selangor 47500, Malaysia

Author contributions: M.C.F., E.H.O., L.M., and M.A. designed research; P.A., I.L., C.V., E.A., F.P., M. Maturi, E.L., S.T., F.C., R.L., and M.O. performed research; M.C.F., E.H.O., L.M., and M.A. contributed new reagents/analytic tools; P.A., I.L., C.V., E.A., B.C., E.L., A.C., J.J., M.C.F., E.H.O., L.M., and M.A. analyzed data; and M. Maturi, E.L., A.S., F.M., M. Moschini, V.P., J.J., M.C.F., E.H.O., L.M., and M.A. wrote the paper.

1. J. Ferlay *et al.*, Cancer incidence and mortality worldwide: Sources, methods and major patterns in GLOBOCAN 2012. *Int. J. Cancer* **136**, E359–386 (2015).
2. E. Comperat *et al.*, Clinicopathological characteristics of urothelial bladder cancer in patients less than 40 years old. *Virchows Arch.* **466**, 589–594 (2015).
3. European Association of Urology, Non-muscle-invasive Bladder Cancer, Chapter 5: Diagnosis. <https://uroweb.org/guidelines/non-muscle-invasive-bladder-cancer/chapter/diagnosis>. Accessed 1 June 2014.
4. P. Zapala *et al.*, Clinical rationale and safety of restaging transurethral resection in indication-stratified patients with high-risk non-muscle-invasive bladder cancer. *World J. Surg Oncol.* **16**, 6 (2018).

5. R. L. Rakesh Heer *et al.*, A randomized trial of PHOTodynamic surgery in non-muscle-invasive bladder cancer. *NEJM Evid.* **1**, EVIDoa2200092 (2022).
6. M. Mossanen, J. L. Gore, The burden of bladder cancer care: Direct and indirect costs. *Curr. Opin. Urol.* **24**, 487–491 (2014).
7. J. Leal, R. Luengo-Fernandez, R. Sullivan, J. A. Witjes, Economic burden of bladder cancer across the European Union. *Eur. Urol.* **69**, 438–447 (2016).
8. A. B. Mariotto, K. R. Yabroff, Y. Shao, E. J. Feuer, M. L. Brown, Projections of the cost of cancer care in the United States: 2010–2020. *J. Natl. Cancer Inst.* **103**, 117–128 (2011).

9. G. Mowatt *et al.*, Photodynamic diagnosis of bladder cancer compared with white light cystoscopy: Systematic review and meta-analysis. *Int. J. Technol. Assess Health Care* **27**, 3–10 (2011).
10. R. O. Draga *et al.*, Photodynamic diagnosis (5-aminolevulinic acid) of transitional cell carcinoma after bacillus Calmette-Guerin immunotherapy and mitomycin C intravesical therapy. *Eur. Urol.* **57**, 655–660 (2010).
11. E. R. Ray *et al.*, Hexylaminolaevulinate fluorescence cystoscopy in patients previously treated with intravesical bacille Calmette-Guerin. *BJU Int.* **105**, 789–794 (2010).
12. F. Del Giudice *et al.*, Systematic review and meta-analysis of vesical imaging-reporting and data system (VI-RADS) inter-observer reliability: An added value for muscle invasive bladder cancer detection. *Cancers (Basel)* **12**, 2994 (2020).
13. A. Saita *et al.*, Assessing the feasibility and accuracy of high-resolution microultrasound imaging for bladder cancer detection and staging. *Eur. Urol.* **77**, 727–732 (2020).
14. L. G. Diana Pietro *et al.*, Head-to-head comparison between high-resolution microultrasound imaging and multiparametric MRI in detecting and local staging of bladder cancer: The BUS-MISS Protocol. *Bladder Cancer* **8**, 119–127 (2022).
15. M. Babjuk *et al.*, European Association of Urology Guidelines on non-muscle-invasive bladder cancer (TaT1 and carcinoma in situ)–2019 Update. *Eur. Urol.* **76**, 639–657 (2019). 10.1016/j.eururo.2019.08.016.
16. E. Alchera *et al.*, Early diagnosis of bladder cancer by photoacoustic imaging of tumor-targeted gold nanorods. *Photoacoustics* **28**, 100400 (2022).
17. I. Steinberg *et al.*, Photoacoustic clinical imaging. *Photoacoustics* **14**, 77–98 (2019).
18. E. H. Ooi, V. Popov, M. Alfano, J. K. K. Cheong, Influence of natural convection on gold nanorods-assisted photothermal treatment of bladder cancer in mice. *Int. J. Hyperthermia* **37**, 634–650 (2020).
19. J. K. Cheong *et al.*, A numerical study to investigate the effects of tumour position on the treatment of bladder cancer in mice using gold nanorods assisted photothermal ablation. *Comput. Biol. Med.* **138**, 104881 (2021).
20. F. Curnis *et al.*, IsoDGR-tagged albumin: A new alphavbeta3 selective carrier for nanodrug delivery to tumors. *Small* **9**, 673–678 (2013).
21. X. Li, J. F. Lovell, J. Yoon, X. Chen, Clinical development and potential of photothermal and photodynamic therapies for cancer. *Nat. Rev. Clin. Oncol.* **17**, 657–674 (2020).
22. S. C. Freitas *et al.*, Key parameters in phototherapy with gold nanorods using continuous near infrared radiation. *Adv. Mater. Interfaces* **10**, 2202214 (2023).
23. A. Abdullahi, S. Amini-Nik, M. G. Jeschke, Animal models in burn research. *Cell Mol. Life Sci.* **71**, 3241–3255 (2014).
24. A. Erman *et al.*, How cancer cells attach to urinary bladder epithelium in vivo: Study of the early stages of tumorigenesis in an orthotopic mouse bladder tumor model. *Histochem. Cell Biol.* **151**, 263–273 (2019).
25. J. Gamrekeshvili, T. F. Greten, F. Korangy, Immunogenicity of necrotic cell death. *Cell Mol. Life Sci.* **72**, 273–283 (2015).
26. T. A. Longo *et al.*, A systematic review of regional hyperthermia therapy in bladder cancer. *Int. J. Hyperthermia* **32**, 381–389 (2016).
27. "American National Standard for safe use of lasers" (ANSI Z136.1–2007, Laser Institute of America, Orlando, FL, 2007; https://research.tcu.edu/wp-content/uploads/2018/12/American-National-Standard-for-Safe-Use-of-Lasers_1.pdf).
28. M. J. Hajipour *et al.*, Sex as an important factor in nanomedicine. *Nat. Commun.* **12**, 2984 (2021).
29. A. Uhlig *et al.*, Gender-specific differences in recurrence of non-muscle-invasive bladder cancer: A systematic review and meta-analysis. *Eur. Urol. Focus* **4**, 924–936 (2018).
30. F. Pederzoli *et al.*, Sex-specific alterations in the urinary and tissue microbiome in therapy-naive urothelial bladder cancer patients. *Eur. Urol. Oncol.* **3**, 784–788 (2020).
31. F. Soria, M. Moschini, S. Korn, S. F. Shariat, How to optimally manage elderly bladder cancer patients? *Transl. Androl. Urol.* **5**, 683–691 (2016).
32. X. Yang *et al.*, The antineoplastic activity of photothermal ablative therapy with targeted gold nanorods in an orthotopic urinary bladder cancer model. *Bladder Cancer* **3**, 201–210 (2017).
33. M. Y. Liao, T. C. Huang, Y. C. Chin, T. Y. Cheng, G. M. Lin, Surfactant-free green synthesis of Au@chlorophyll nanorods for NIR PDT-elicited CDT in bladder cancer therapy. *ACS Appl. Bio Mater.* **5**, 2819–2833 (2022).
34. N. A. Virani *et al.*, Phosphatidylserine targeted single-walled carbon nanotubes for photothermal ablation of bladder cancer. *Nanotechnology* **29**, 035101 (2018).
35. K. Shin *et al.*, Cellular origin of bladder neoplasia and tissue dynamics of its progression to invasive carcinoma. *Nat. Cell Biol.* **16**, 469–478 (2014).
36. P. J. Goebell, M. A. Knowles, Bladder cancer or bladder cancers? Genetically distinct malignant conditions of the urothelium. *Urol. Oncol.* **28**, 409–428 (2010).
37. I. Z. Yildiz *et al.*, Utility of a dual immunostain cocktail comprising of p53 and CK20 to aid in the diagnosis of non-neoplastic and neoplastic bladder biopsies. *Diagn. Pathol.* **4**, 35 (2009).
38. Q. Li *et al.*, Expression and correlation of Lewis y antigen and integrins alpha5 and beta1 in ovarian serous and mucinous carcinoma. *Int. J. Gynecol. Cancer* **20**, 1482–1489 (2010).
39. H. Y. Wang, Z. Chen, Z. H. Wang, H. Wang, L. M. Huang, Prognostic significance of alpha5beta1-integrin expression in cervical cancer. *Asian Pac. J. Cancer Prev.* **14**, 3891–3895 (2013).
40. K. A. Lombardo *et al.*, Urothelial carcinoma in situ of the bladder: Correlation of CK20 expression with adaptive immune resistance, response to BCG therapy, and clinical outcome. *Appl. Immunohistochem. Mol. Morphol.* **29**, 127–135 (2021).
41. F. Pederzoli *et al.*, Diagnosis of urothelial carcinoma in situ using blue light cystoscopy and the utility of immunohistochemistry in blue light-positive lesions diagnosed as atypical. *Hum. Pathol.* **90**, 1–7 (2019).
42. M. Babjuk *et al.*, European association of urology guidelines on non-muscle-invasive bladder cancer (Ta, T1, and carcinoma in situ). *Eur. Urol.* **81**, 75–94 (2022).
43. European Association of Urology, Non-muscle-invasive Bladder Cancer, Chapter 7: Disease Management. <https://uroweb.org/guidelines/non-muscle-invasive-bladder-cancer/chapter/disease-management>. Accessed 1 June 2014.
44. C. Tholomier, L. Souhami, W. Kassouf, Bladder-sparing protocols in the treatment of muscle-invasive bladder cancer. *Transl. Androl. Urol.* **9**, 2920–2937 (2020).
45. M. Alfano, Gold nanorod-assisted theranostic solution for non-visible residual disease in bladder cancer. San Raffaele Open Research Data. <https://doi.org/10.17632/bwbsk2wr3z.1>. Deposited 20 August 2024.